Superconducting single photon detectors, magnetic fields and polarisation

THESIS

submitted in partial fullfillment of the
requirements for the degree of

MASTER OF SCIENCE

in

PHYSICS

Author :   Irina Komen
Student ID :   0916110
Supervisor :   Jelmer Renema
                            Martin van Exter
2nd corrector :   Jan Aarts

Leiden, The Netherlands, March 28, 2014

Superconducting single photon detectors, magnetic fields and polarisation

Irina Komen

Huygens-Kamerlingh Onnes Laboratory, Leiden University
P.O. Box 9500, 2300 RA Leiden, The Netherlands

March 28, 2014

Abstract

We study the behavior of superconducting single photon detectors in magnetic fields as well as their response to photons of different polarisation. We find two regimes in the critical current of the detector as a function of magnetic field, namely a regime of induced depairing and a flux flow regime. For higher magnetic fields, dark counts dominate. Dark counts are only observed at currents close to the critical current, whereas light counts follow a different current scale. We find the same two regimes in the observed light count rates as in the critical current. In the first regime with low magnetic fields, light counts of SSPDs can be described using the solution of the Usadel equation in the homogeneous case. Besides, we also study the response of SSPDs to light of different polarisations. This leads to a better understanding of the detection process as a well as the position of where the photons are absorbed by the detector.

Contents

Chapter 1

Introduction

Superconductivity was discovered in 1911 by Kamerlingh Onnes [1]. A promising application of superconductivity are superconducting single photon detectors (SSPDs). These detectors were invented in 2001 by Gol'tsman [2]. They show high efficiencies over 90% [3], have a small jitter of about 10 ps [2], low dark counts of a few per second and high light count rate of tens of MHz. SSPDs perform in a broad wavelength range of 200 nm to 2000 nm. Their main application is in the infrared, where due to the combination of favorable features, these devices outperform their alternatives in many ways [4].

A typical SSPD consists of a meander of a superconducting film. The film has a thickness of a few nanometers, so the material can be seen as two dimensional. SSPDs are biased to a large fraction of the critical current. Absorption of a photon will result in the creation of an avalanche of quasi particles. This eventually results in the formation of an area in the material where the superconductivity is destroyed. This will have a resistance, which can easily be measured as a voltage pulse [5]. In this way, the response of the SSPD to photons is detected and the superconductor can be used as a single photon detector.

Because of their outstanding performance, SSPDs have many possible applications. They can be used in quantum key distribution, optical quantum computing, characterization of quantum emitters like quantum dots and molecules at infrared wavelengths, space to ground communication, integrated circuit testing, fibre temperature sensing and time of flight depth ranging of LIDAR systems [4].

However, the underlying physics of these detectors is not fully understood. Many open questions remain, involving the behavior of both dark and light counts. As superconductivity is intrinsically influenced by magnetism, and magnetism also plays a role in the detection mechanism of photons in SSPDs, interesting information about the physics in SSPDs could be obtained by investigating their behavior in a magnetic field. Recently, both dark and light counts in a magnetic

1

field have been studied on technologically relevant meander samples [6]. Questions remain about the behavior of the critical current as a function of magnetic field, but also on whether these detectors behave purely as superconductors, or whether their behavior is changed by effects related to the photodetection. Therefore, studying the critical current, dark counts and light counts of SSPDs in a magnetic field provides information about their working mechanism and the physics involved.

Information about the physics of SSPDs is also gained by looking at their response to light of different polarisations. This leads to a better understanding of the detection process [7]. The probability for photons to be absorbed at some position of the wire depends on their polarisation. Further, the probability that the detector clicks depends on the position where the photon was absorbed. Therefore varying the polarisation provides a way of acquiring information about the relationship between the position where the photon is absorbed, its absorption probability and its click probability.

This thesis consists of eight chapters. After the introduction, Chapter 2 reviews some superconductivity, explains in more detail about superconducting single photon detectors and the method of detector tomography. Chapter 3 provides information on the used samples, the electronics and a description of our setups. Then Chapter 4 states the results for the magnetic field experiments, involving critical current, dark counts and light counts, and Chapter 5 provides a discussion on these results. Chapter 6 proceeds with the results for the polarisation experiments, where Chapter 7 provides a discussion on these results and the thesis ends with a conclusion.

Chapter 2

Theory

2.1 Superconductivity

There are two key phenomena that define a superconductor. The first key property of a superconducting material is that its resistivity becomes exactly zero below a certain critical temperature [1, 8]. This critical temperature T_c depends on the material. Experiments have been done where a current is set up in a closed loop of superconducting wire. Even on a large time interval of two years, this current does not dissipate. This demonstrates that the resistivity of a superconductor becomes exactly zero [8].

The second defining property of superconductivity is related to magnetism. Superconductors expel magnetic fields when they are below their critical temperature. This happens irrespective of whether the magnetic field is first applied to the superconductor, which is then cooled down below its critical temperature, or whether the magnetic field is applied to a material which is already superconducting. The expulsion of the magnetic field by a superconductor is called the Meissner effect. A magnetic field does enter a superconducting material, but it decays exponentially with the London penetration depth λ. This leads to a set of phenomenological equations, describing the behavior of current and magnetic field in a superconductor, namely the London equations [1, 8].

There are two other theories for superconductivity. The first is the Ginzburg-Landau theory, which explains phenomena in a more quantum mechanical and thermodynamical way. In this theory, the superconducting electrons are described by a complex wave function Ψ, where $|\Psi|^2$ gives the density of superconducting electrons [1]. Related to this wave function is the coherence length ξ, which is the typical length over which Ψ can vary. This wave function Ψ is also called the superconducting order parameter. It is zero in the disordered or normal state of the metal, and has some value in the superconducting state [8]. Ginzburg-Landau

theory is only valid for temperatures around the critical temperature. Although the Ginzburg-Landau theory does not start from first principles, almost all superconducting phenomena can be explained using this theory.

The second theory for superconductivity is the microscopic BCS (Bardeen, Cooper, Schrieffer) theory. Here the electrons in a superconductor are interacting with each other in pairs, which are called Cooper pairs. A possible interaction mechanism is via phonons in the lattice. It is energetically more favorable for electrons near the Fermi surface to have an attractive interaction in pairs, instead of proceeding as individual electrons. The electrons forming a Cooper pair should have equal and opposite momenta and spin [1]. When a current is running through a superconductor, the electrons do scatter like they do in a normal metal. However, as the sum of the momenta of the electrons in the Cooper pair is conserved, the total current running through the device does not experience resistance. In this way, BCS theory explains the absence of resistance in a superconductor based on the interaction of Cooper pairs in the material.

BCS theory states that not unlike semiconductors, superconductors have a bandgap. The behavior of a semiconductor can be described by having a lower and a higher band with a gap in between, where electrons can be excited to the higher band. The energy that is needed to excite the electron is given by the size of the bandgap. Superconductors can be described in the same way, where the size of the bandgap depends on the temperature. The bandgap 2Δ is given by the amount of energy needed to break a Cooper pair [1].

There is also an analogy between superconductivity and Bose-Einstein condensation. Electrons are fermions, but Cooper pairs are bosons. In the ground state, these bosons all condense into the same state. Therefore superconductivity has a macroscopically occupied groundstate [1].

There are two things that can weaken and even break the superconductivity, namely current and magnetic field. Soon after the discovery of superconductivity, it was found that there is a limit to the current that can be driven through a superconductor. Driving a current through a superconductor makes the size of the bandgap smaller, so part of the Cooper pairs is broken apart. Therefore, above a certain critical current the superconductor starts having a resistance [1].

Superconductivity can also be weakened by a magnetic field, although this happens differently for different types of superconductors. In type I superconductors, the superconductor expels the magnetic field as much as possible over a length scale λ, until above a certain critical field the superconductivity is destroyed [8]. Type II superconductors do allow magnetic field inside, but quantized in vortices. In a vortex, the magnetic field is confined to pointlike spots surrounded by shielding currents. In type II superconductors there are two critical fields. At H_{c1}, the superconductor goes into a state where there is a combination of superconducting and normal regions. The material loses more and more of its

superconductivity, until at H_{c2} it has become a normal material [1]. Abrikosov found that in the intermediate mixed state, the magnetic flux penetrates into the superconductor in a regular lattice of vortices. Each vortex consists of a magnetic, non-superconducting core with a shielding current around it [9]. This means that the magnetic field weakens superconductors by trying to penetrate inside, either at the edges of the material in type I superconductors, or by means of vortices in type II superconductors.

The distinction between type I and II superconductors is given by comparing the London penetration depth with the coherence length. The coherence length ξ of the Ginzburg-Landau theory also has a meaning in BCS theory. It is the length at which there still are correlations between two electrons forming a Cooper pair [1]. It is also related to the size of the pieces of material which become normal due to current or magnetic field. The London penetration depth λ gives the degree over which the edges of the material are shielding the magnetic field. In type II superconductors, where $\lambda > \xi$, it is energetically favorable that small parts of the material are normal, but the shielding is very strong. In type I superconductors, where $\lambda < \xi$, it is energetically favorable that the shielding is low, and the material becomes less superconducting over a large area. Thus in type II superconductors vortices are formed, and in type I not.

For our experiments, a relevant way of looking at superconductivity is by the Usadel equations [10]. These equations describe parameters such as the Density of states or the critical curent, in a position-dependent way and at all temperatures. This theory is applicable only for superconductors in the dirty limit, where the electron mean free path is shorter than the coherence length of the Cooper pairs. The main idea of this theory is that in this limit, bias current and magnetic field have the same pair breaking effect on Cooper pairs, so the two are interchangable. All physical quantities in the Usadel equations only depend on the combination [10]

$$\vec{\nabla}\phi - (2e/\hbar)\vec{A}, \tag{2.1}$$

where the gradient of the phase of the superconducting order parameter, $\vec{\nabla}\phi$, is associated with the current and $\vec{A}$ is the magnetic vector potential. This shows the equivalence of current and magnetic field.

From the Usadel equations, the following relationships can be extracted [10]:

$$\frac{\hbar D}{2}\nabla^2\theta + [iE - \frac{\hbar}{2D}\vec{v}_s^2 cos\theta]sin\theta + \Delta cos\theta = 0, \tag{2.2}$$

where D is the diffusion coefficient, the complex function $\theta(\vec{r}, E)$ is the pairing angle that describes the correlations between electrons of opposite spin and

momenta, E is the energy, $\vec{v}_s$ is the superfluid velocity and Δ is the pairing potential. Here [10]:

$$\vec{\nabla}(\vec{v}_s sin^2\theta) = 0. \tag{2.3}$$

In a homogeneous situation, an approximation was made by Anthore [10]. The theory is then able to describe the current, temperature and field dependence of the superconducting gap by a single parameter Γ, called the depairing energy:

$$\frac{\Gamma}{\Delta_0} = (\frac{\Delta_0}{U_S(\Gamma)}\frac{I_s}{I_\Gamma})^2 + (\frac{B}{B_\Gamma})^2, \tag{2.4}$$

where Γ is the depairing energy, Δ_0 is the bandgap at zero temperature, I_s is the bias current and B is the applied magnetic field. In this equation, $I_\Gamma = \sqrt{2}\Delta_0 L/(eR\xi_0)$ and $B_\Gamma = \sqrt{6}\hbar/(ew\xi_0)$. Here R is the resistance of the wire, ξ_0 is the coherence lenght at zero temperature, L is the length and w is the width of the wire. U_s is related to the superconducting charge density abailable for carrying supercurrent, and therefore depends on Γ.

At $k_B T << \Delta$, the following approximation is valid:

$$\frac{U_S(\Gamma)}{\Delta_0} \simeq \pi/2 - 1.8\frac{\Gamma}{\Delta_0} - 1.0(\frac{\Gamma}{\Delta_0})^2. \tag{2.5}$$

2.2 Superconducting single photon detectors

2.2.1 Photodetection mechanism

It is known that the absorption of a photon in an SSPD results in the local breaking of the superconductivity. However, there exist different theories about the exact way in which the superconductivity is destroyed by the photon. Recently, a large class of models could be experimentally excluded [11]. In the model which gives predictions that correspond most to the measured data, mirror vortices are formed to compensate for the formed vortices and hence to satisfy the electromagnetic boundary conditions [12]. When a photon is absorbed, some of the Cooper pairs break up into electrons, which scatter and break up more Cooper pairs. This happens faster than the recondensation of the electrons. In this way, in part of the material the superconductivity is broken, and the diffusing cloud of electrons expands. Due to this cloud, the current density near the edges of the wire is changed, which decreases the energy barrier for the vortex entry. The bias current will cause a Lorentz force on the vortex, which will cross the wire. This will trigger the formation of a normal and resistive slab of material, which can be detected.

2.2.2   Influence of magnetic field

As mentioned before, superconductors in general respond to a magnetic field by expelling it. Above a certain field, it is thought that magnetic vortices are allowed inside. These vortices are involved in the production of both dark counts as well as photon counts in superconducting detectors. This makes studying the effects of a magnetic field on a SSPD an interesting topic. From a more technological point of view, applying a magnetic field to an SSPD might lead to higher detection efficiencies.

2.2.3   Influence of polarisation

Another experimentally interesting phenomenon to look at, is the detector response for different polarisations of the light. Here it is important to distinguish the absorption of the detector from the probability that the detector clicks, provided that a photon is absorbed. A large difference in absorption between light of different polarisations is reported for meanders [13, 14].

We are interested in the influence of polarisation on our short and long wire samples. Due to electromagnetic boundary conditions, the polarisation is predicted to affect the position in the wire where the photon is most likely absorbed. Photons with a parallel polarisation can be absorbed anywhere in the wire. However, photons with a perpendicular polarisation have a higher probability to be absorbed in the middle of the wire, and not near the edges (see Figure 2.1).
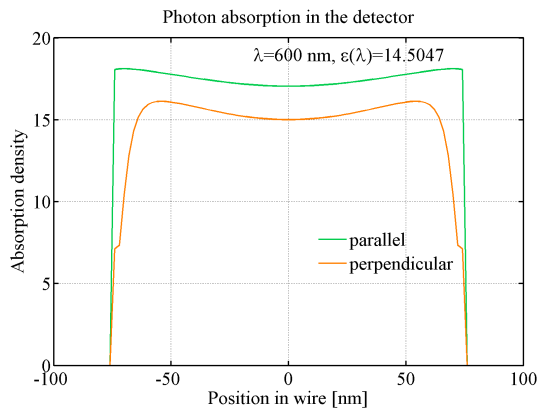
Figure 2.1: *FDTD calculation of the absorption of light as a function of position, calculated in a relevant geometry by Q. Wang [15]. Here the width and the length of the wire both are 150 nm. The absorption of light with parallel absorption is nearly constant through the wire, but light with perpendicular polarisation is less absorbed in the edges than in the middle.*

Important to mention is that the absorption probability as a function of position in the wire is predicted to depend on wavelength. The absorption probability depends on the dielectric constant. Since the dielectric constant of the material we use, NbN, is strongly wavelength dependent, the same wavelength dependence is present in the absorption probability.

Furthermore, the polarisation is also predicted to affect the position in the wire where the photon is most likely to induce a detection event, once it is absorbed (see Figure 2.2) [7]. This is because when a photon is absorbed near the edge of the wire, the current distribution near the edge is affected much more than when the photon is absorbed in the middle. The current distribution affects the energy barrier for the vortex to enter, which causes the detection event. Consequently, when a photon is absorbed near the edge, the click probability is much higher than when it is absorbed in the middle.
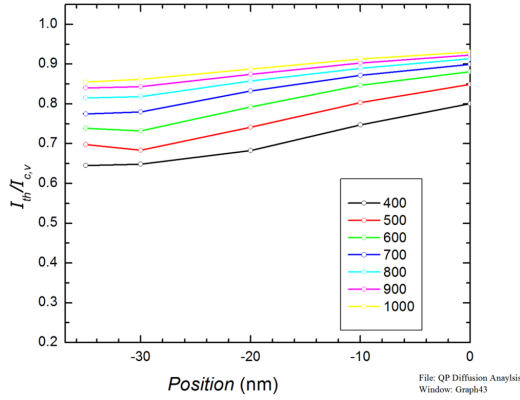
Figure 2.2: *Reduced current as a function of position on the wire for different wavelengths. The reduced current is the threshold bias current introduced by Engel [16], divided by the current scale in the vortex model [16]. The current distribution affects the click probability. In the middle of the wire, this current is higher than at the edge. For shorter wavelengths, this effect is larger than for high wavelengths.*

Important to note is that the dependence of click probability on the position of the absorbed photon in the wire, and thus on the polarisation of the photon, is predicted to be wavelength dependent [7]. For shorter wavelengths, the difference between the polarisations should be larger (see Figure 2.2).

2.3 Detector tomography

To understand the underlying physics of a single photon nanodetector, it is necessary to characterize it. The goal in characterizing the detector is to find the

probability that it clicks as a function of the number of impinging photons. The method to do this is described below and proposed by Renema et al [17]. Ideally, we would want to have the response of the detector in the Fock (number) state basis. This would allow a description of the response of the detector to a given amount of photons. Since there are no sources available which produce light in this basis, we use coherent light of a laser. Coherent light can be decomposed in the number state basis using the mean photon number, which can simply be determined by measuring the intensity of the light.

However, there are two factors which make understanding the physics of the detection process more complicated. Nanodetectors are multiphoton detectors which react on different numbers of photons in some nontrivial way. Moreover, there is also a probability that a photon does not get absorbed in the detector, so there are losses in the detection process. Using detector tomography, the regimes where the detector reacts on different numbers of photons can be distinguished. Also the linear loss and the nonlinear detection mechanism inside of the detector can be separated. Hence, detector tomography is a suitable tool to characterize a quantum photon detector.

Doing tomography, we measure the photon counts as a function of the laser intensity. From the photon counts we extract the probability per laser pulse that the detector clicks, R_{click}, by dividing it by the repetition rate of the laser. From the intensity, we extract the mean photon number by using the power and the repetition rate of the laser. Because the laser produces coherent light,

$$R_{click}(N_{in}) = \sum_{i=0}^{\infty} P_i e^{-N_{in}} \frac{N_{in}^i}{i!}. \tag{2.6}$$

Here P_i is the probability that the detector first absorbs a photon and then clicks, and N_{in} is the number of incident photons.

There are only two possibilites in this detector, namely click or no click. This means the following:

$$R_{click}(N_{in}) = 1 - R_{noclick}(N_{in}), \tag{2.7}$$

$$R_{click}(N_{in}) = 1 - e^{-N_{in}} \sum_{i=0}^{\infty} (1 - P_i \frac{N_{in}^i}{i!}). \tag{2.8}$$

These formulas are applicable to any one photon detector with two possible outcomes.

Traditional tomography is based on the number of incident photons. In [17], this was modified to a description in terms of the number of photons absorbed by the device. To separate the linear losses from the nonlinear detection mechanisms

in the detector, we introduce a linear loss parameter η. We add this to the formula, which can be done because coherent states remain coherent under attenuation and losses:

$$R_{click}(N_{abs}) = 1 - e^{-\eta N_{abs}} \sum_{i=0}^{i_{max}} (1 - p_i) \frac{(\eta N_{abs})^i}{i!}), \qquad (2.9)$$

where p_i is the probability that the detector absorbs a photon without the click probability included and N_{abs} is the number of absorbed photons. Now we have added a parameter to the description and by this created overdetermination. This means we can choose the value of some of the other parameters. It is physically reasonable to assume that for large numbers of photons, the detector will click anyway, so $p_{i_{max}} = 1$ and all $p_{j>i_{max}} = 1$ as well.

Finally, we can use this formalism to reconstruct the η and p_i's of our detector. We do this by fitting our data to Equation 2.9. We pick the solution which fits best and uses the smallest number of parameters, because we expect this to be physically most realistic. From this fit we extract the values of η and p_i [17].

Chapter 3

Methods

3.1 Samples

To study the underlying physics of superconducting single photon detectors, using a detector with only one active area instead of a meander has several benefits [18]. In the response of a meander detector to photons, geometrical effects like current crowding in its turns will play an important role [19]. Moreover, large variations have been seen in detection efficiencies between nominally identical devices. These variations were attributed to constrictions, where the width of the wire is reduced due to inhomogenities and production mistakes [20]. Multiphoton behavior is also difficult to study with a meander, because situations of two photons being absorbed near each other in the same meander arm are much less likely than two photons being absorbed in different places of the meander, which will result in two single photon responses. Therefore, to study the exact behavior of superconducting photon detectors, a detector with only one active area is more appropriate than a meander. Such a device consists of a single nanoscale constriction in a wire with meander inductors on both sides. It will not suffer from geometrical effects and constrictions, and photons will be detected only in the narrow part of the sample.

We performed our measurements on three detectors, patterned on a 5 nm thick NbN film on a GaAs substrate and fabricated in the group of A. Fiore in Eindhoven University of Technology. The first sample had a constriction of 220 nm wide in the wire. This is further on called nanodetector (see Figure 3.1a) [18]. The second and third samples were short wires of 150 nm width and 100 nm or 200 nm length (see Figure 3.1b and 3.1). Around these constriction and short wires a meander is patterned of 16 wires with a width of 500 nm and a length of 38 μm. We performed the measurements in the magnetic field on the nanodetector and the short wire of 200 nm lenght, and the polarisation dependent measurements on the

short wire of 100 nm length. The relevant values of other physical constants for our samples are given in Table 3.1. Here the critical temperature and the value of ξ_0 were measured only on the short wire. The resistance is a rough estimation from measurements of resistance as a function of temperature.

	nanodetector	short wire
critical temperature T_c	~ 9.5 K	9.5 K
resistance R	~ 500 $k\Omega$	~ 700 $k\Omega$
length L (16 wires of 38 μm)	0.608 mm	0.608 mm
width w	220 nm	150 nm
width of surrounding wires w_0	500 nm	500 nm
ξ_0	~ 3.9 nm	3.9 nm
$\Delta_0 = 2.07 k_B T$	$2.715 * 10^{-22}$ J	$2.715 * 10^{-22}$ J
$I_\Gamma = \sqrt{2}\Delta_0 L/(eR\xi_0)$	329 μA	160 μA
$B_\Gamma = \sqrt{6}\hbar/(ew\xi_0)$	1.879 T	2.756 T

**Table 3.1:** *Relevant values of physical constants for our samples.*

3.2   Electronics

The relevant quantity to measure on an SSPD are counts as a function of bias current. Measuring the voltage over a resistance provides additional information about its superconducting behavior. A sketch of the used electrical circuit is shown in Figure 3.2. The detector is voltage biased by a Yokogawa GS200 voltage source. A bias-T is used to separate this DC voltage from the AC signal,

(a) Nanodetector

(b) Short wire 1.
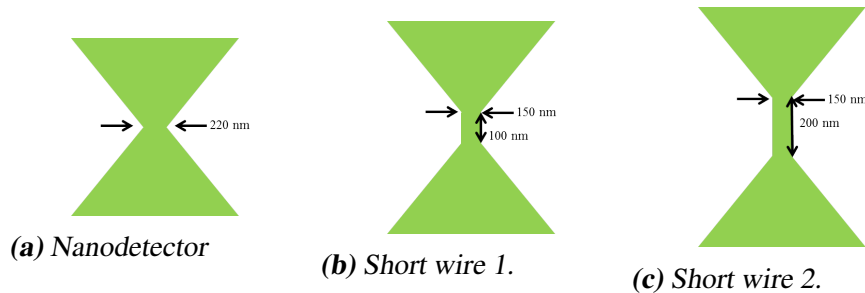
(c) Short wire 2.

Figure 3.1: *The samples we used were: (a) a nanodetector of 220 nm width, and two short wires of 150 nm width (b) one 100 nm length, (c) the other 200 nm length.*

produced by the detector. In the DC arm of the circuit, the voltage over a 100 Ω resistance is measured using an Agilent voltmeter 34410A for the magnetic field measurements and a Keithley voltmeter 2000 for the tomography measurements. The AC signal from the detector is amplified and detected by an Agilent pulse counter 53220A or 53131A. In this way, the counts and the output voltage are measured as a function of the input voltage.
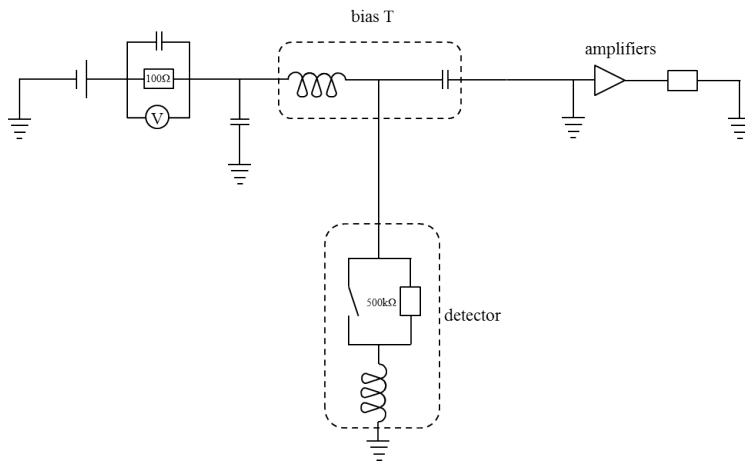
Figure 3.2: *Sketch of the used electrical circuit.*

In the magnetic field setup, a large electronic problem is caused by multiple grounds with different potentials. This was partially solved by adding grounding cables and an additional grounding device to the set-up (see also [21]).

3.3   Magnetic field setup

To measure the influence of a magnetic field on the detector, the sample is placed on an insert, which is mounted in a cryostat. The insert consists of a tube of steel, with electronic cabling, a multimode laser fiber and mechanical feedthroughs to align the laser (see [22] for a more extensive description).

The cryostat used is a Physical Property Measurement System (PPMS). The temperature can be set to any value from 1.8 K to room temperature (see [22] for an extensive description of the PPMS and the heat flow inside). The device is able to produce magnetic fields up to 9 T.

3.4 Tomography setup

For the tomographic measurements, we used a Fianium supercontinuum laser. This laser has an emission spectrum from 400 nm to 2400 nm. Dielectric filters can be used to select a certain wavelength band, but they have limited transmission and blocking bands. The edgepass filters we used are specified from $0.7\lambda_c$ to $1.3\lambda_c$, where λ_c is the cutoff wavelength. For this reason, a series of filters is needed to select a small wavelength band out of the continuum (see Figure 3.3 for a sketch of our setup). First, a wavelength range of 300 nm is selected using a combination of short- and longpass filters. Then, a bandpass filter is inserted to select a wavelength with a band of around $\delta\lambda$=10 nm. For visible wavelengths, an additional FGS900M filter was used. To provide additional filtering, we used dielectric mirrors (E02 and E03 coating from Thorlabs) as an additional wavelength-selective element. With this setup, we typically achieved suppression of the undesired wavelengths of optical density 7.

Figure 3.3: *Sketch of our setup.*

The cryostat that we used for the tomography setup is a two stage pulse tube cryocooler, model SRP-062. It has a base temperature of 3.1 K.

To perform tomographic measurements, it is necessary to illuminate the sample in the cryostat with laser light, so to transport the light from the laser to the sample. Our sample was mounted at the top of the cryostat, so we put a mirror inside to reflect the light onto the sample. All other optics was located outside of the cryostat, so it could be controlled and adjusted. To translate the light from the level of the laser to the level of the window of the cryostat, we used a combination of two mirrors in a periscope configuration. To get control over both angle and position of the light beam on the sample, which are four degrees of freedom, at least two mirrors are needed. To transport the light from the laser to the sample, we used an additional three mirrors. As alluded to before, we used two dielectric mirrors. All other mirrors were metallic (P01). In this way the light from the laser was transported to the sample.

The light on the sample should be focused. A combination of two lenses forming a telescope was used to make the beam parallel. Then a lens focused the beam on the second mirror. A last lens imaged the focus of the beam from the mirror on the sample. In order to be able to look at the shape and position of the beam, we used a beam splitter to image the reflected light from the sample on a camera.

As discussed previously, for doing tomography the response of the detector has to be measured as a function of different laser intensities. To measure at different laser powers in a controlled way, we used a combination of a polarizer, a half-wave plate and another polarizer, and rotated the half-wave plate over 45 degrees. The half-wave plates were specified for a wavelength range of 400 nm to 800 nm or 690 nm to 1100 nm. We used Glan Thompson polarizers. Afterwards, we performed a calibration measurement, measuring powers as a function of angles of the half-wave plate with a power meter. In that way we obtained the photon counts as a function of the laser power.

To set the polarisation of the light on the sample, we added an extra half-wave plate after the second polarizer and rotated it over 90 degrees. The half-wave plates are controlled using a Newport motion controller ESP300.

4 | Chapter

Results for magnetic field experiments

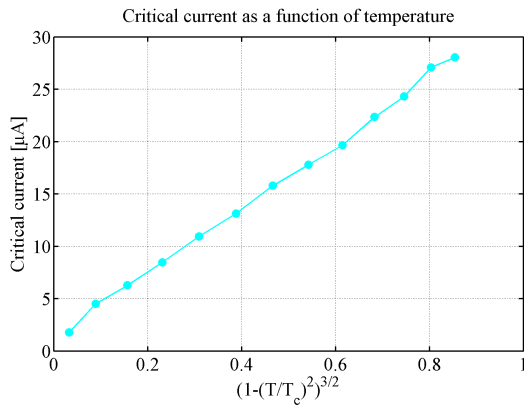## 4.1 Critical current on nanodetector

Figure 4.1 shows the critical current of the nanodetector as a function of the magnetic field. To extract the critical current from our data, we used a 10% resistance criterion. The resistance at zero bias current was 100 Ω, which is only the resistance of the resistor in the circuit (see Section 3.1). This means we had a threshold criterion of 100 + or - 10 Ω for determining the critical current. Using a step size of 0.025 mV resulted in a resolution of approximately 1 Ω. For low fields, the critical current depended linearly on the magnetic field. For higher fields above 50 mT, the dependence was a power law $I_c \sim B^x$.

(a)   **(b)**
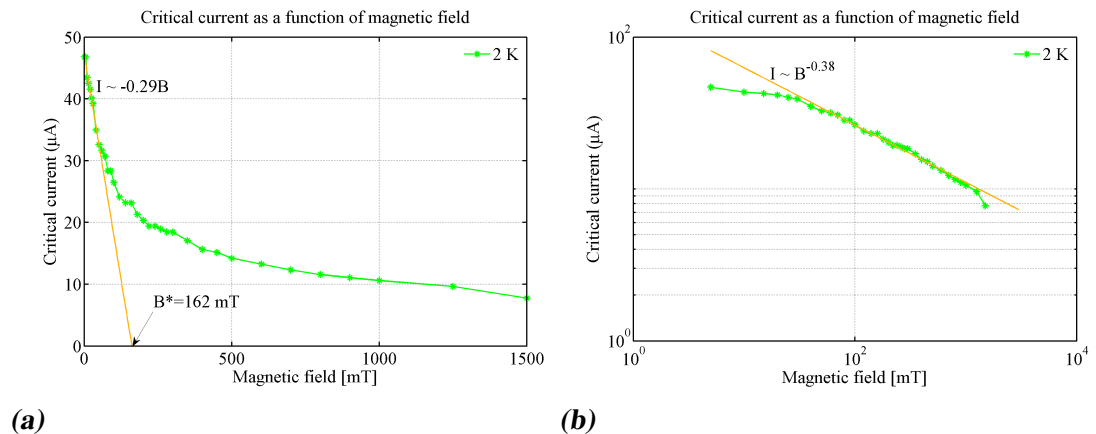
Figure 4.1: *Critical current as a function of magnetic field on a normal and on a log-log scale at a temperature of 2K on the nanodetector. The first part of the curve is linear, and for fields above 50 mT it obeys a power law.*

4.1.1   Temperature dependence

The critical current as a function of magnetic field was measured at different temperatures. The critical current for zero magnetic field obeyed a Bardeen temperature dependence (see Figure 4.2) [23]. The interception of the linear fit with the B axis, B*, varied with temperature between 144 mT at 5.5 K and 162 mT at 2 K. The slope of the linear part was -0.29 $\mu A/mT$ for 2 K and -0.19 $\mu A/mT$ for 5.5 K. The second part of the curve obeyed a power law $I_c \sim B^x$, where x = -0.39 for 2K and x = -0.84 for 5.5K.


Figure 4.2: *Critical current for zero magnetic field as a function of temperature for a meander sample. It obeys the Bardeen temperature dependence [23].*
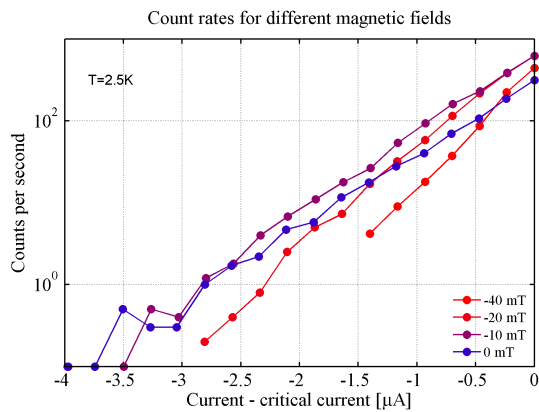
4.2   Dark counts on nanodetector

First, measurements of dark counts were performed with the laser off. These dark counts increased exponentially with current as $R_{dark} \sim e^{I/\alpha}$ (see Figure 4.3). For increasing field, the dark count curve maintained its shape but shifted to lower currents. The exponent α = 2 μA for 0 mT and α = 3.5 μA for 50 mT. The dark counts become easily measurable (R >1 /s) at 90% of the critical current and followed it precisely. Plotting the dark counts as a function of $I - I_c$ resulted in an approximate overlapping of the curves (see Figure 4.4). Note the difference in scale from Figure 4.3. Here the point of $I - I_c = 0$ means a point within a measurement step away from the critical current. At exactly the critical current, the counts become of the order of 10^6.

Dark counts as a function of current in the short wire had the same exponential shape and showed similar behavior for different magnetic fields.
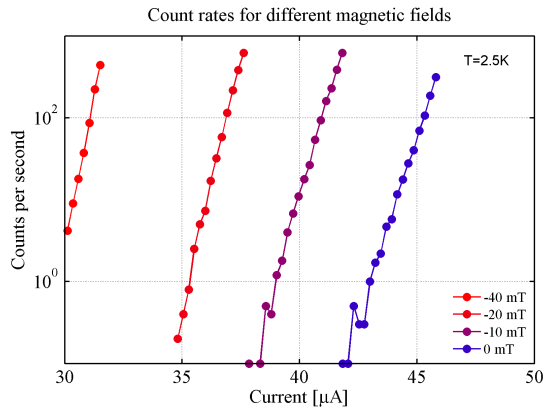
Figure 4.3: *Dark counts as a function of current show exponential behavior. This particular curve is for the nanodetector. For different magnetic fields, the curves shift towards lower currents. Dark counts become easily measurable at 90% of the critical current. Here the point of $I-I_c$=0 means a point within a measurement step away from the critical current. At exactly the critical current, the counts become of the order of 10^6.*
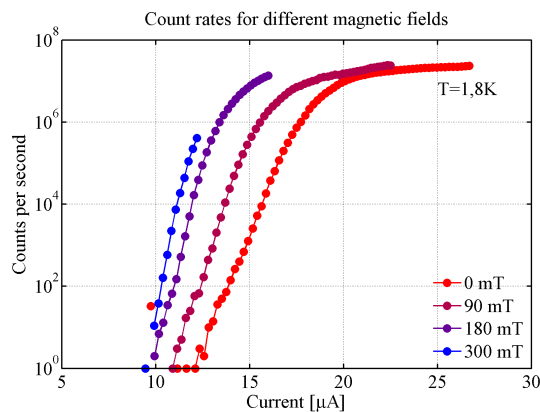

Figure 4.4: *Dark counts as a function of $I - I_c$ on the nanodetector. As dark counts follow the critical current, the curves approximately fall on top of each other. Note the difference in scale from Figure 4.3.*

4.3 Light counts on short wire

Light counts were measured as a function of current on a short wire. Light with a wavelength of 826 nm was used at fixed intensity (see Figure 4.5). It has been reported before [6], that the shape of the curve of the light counts is totally different from the exponential shape of the dark counts. The light counts become easily measurable at around 50% instead of 90% of the critical current. The curves start off exponentially and then flatten out to a plateau regime. The exponent α was of the same order of magnitude as that of the dark counts, although its exact value depended on where the crossover point between the exponential and flatter part was chosen. For different magnetic fields, the curves were shifted towards lower currents. At the same time, the flatter part of the curves becomes smaller and disappeared at last.

The same two regimes were observed in the light counts in the nanodetector, namely an exponential and a plateau regime. Light counts in a nanodetector show similar behavior for different magnetic fields, where the curves shift towards lower currents and the flatter part becomes smaller and disappears for higher fields.
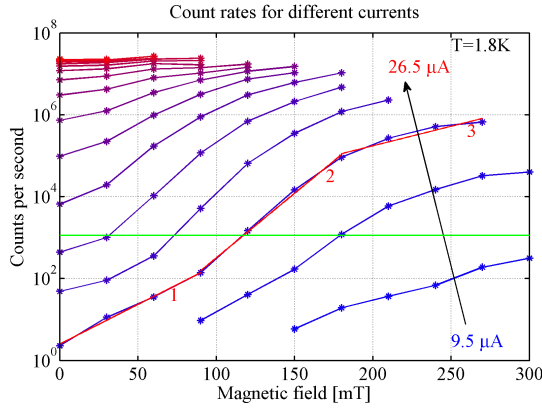

Figure 4.5: *Light counts as a function of current for different magnetic fiels. This particular curve is for the short wire 2. Light counts behave in a different way than dark counts. The light counts become easily measurable at 50% of the critical current and first show exponential behavior, where after a certain point the curve flattens out. For different magnetic fields, the curves shift towards lower currents and lose their flat part.*

4.4 Light counts and magnetic field

In Figure 4.6, these data can be represented in another way, namely with light counts as a function of magnetic fields for different currents. The curves certainly

do not show single exponential or cosh like behavior, which was predicted in the literature [12]. We can distinguish three regimes with different exponential behavior $R \sim e^{B/\beta}$. For low fields below 50 mT, β = 22.4 mT for regime 1. For higher fields between 50 mT and 200 mT, β = 13.8 mT for regime 2. For fields higher than 200 mT, where the counts are near the critical current, β = 45.4 mT for regime 3.


Figure 4.6: *Light counts represented as a function of magnetic field on short wire 2. For different currents, these curves shift towards higher counts. Three regimes can be seen where the slope is different. The red fits 1, 2 and 3 are fits of the three regimes of the curve for 12.5 μA. The green line indicates the data points with a constant countrate of 1000 counts per second.*

4.5   Usadel on short wire

In Figure 4.7, current is plotted as a function of magnetic field for a constant count rate of 1000 counts (see green line in Figure 4.6). We fitted the Anthore approximation to the Usadel equation to these data (see Section 2.1, Equation 2.4), and it fits well up to 50 mT (see Figure 4.7). This was the case at all the temperatures we measured at. To fit the equation we calculated I_Γ=160 μA and B_Γ=2.756 T (see Table 3.1), and used Γ/Δ as the only free parameter. In Figure 4.7 this means that the shape of the ellipse is fitted, i.e. the ratio between the B and the I axis is fixed, but the size of the ellipse is freely adjustable. For higher fields, it did not fit any more (see Figure 4.8). For fields higher than 200 mT, the current as a function of magnetic field for constant countrate followed the critical current. We attribute this to a dominance of dark counts under these conditions (see Discussion, Section 5.2).
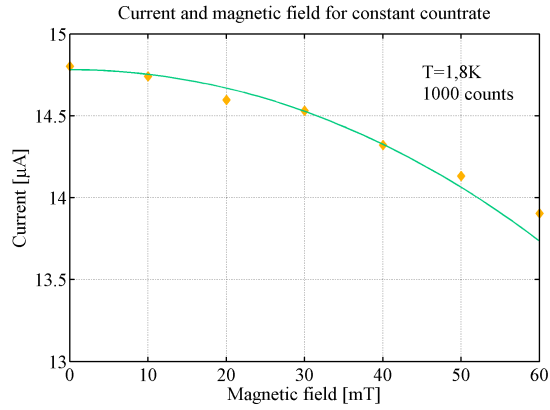
Figure 4.7: *Current as a function of magnetic field for a constant countrate of 1000 counts per second on short wire 2 (see green line in Figure 4.6). The first data points are fitted with Equation 2.4, where I_Γ=160 μA and B_Γ=2.756 T. The only free parameter is Γ/Δ.*
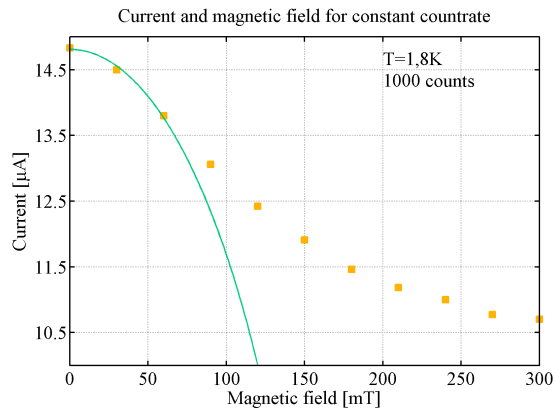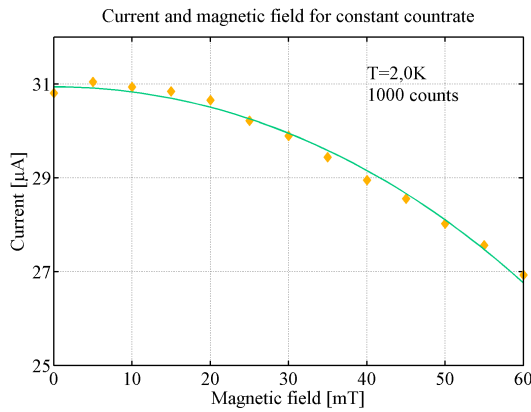

Figure 4.8: *Current as a function of magnetic field for a constant countrate of 1000 counts per second on short wire 2. The data are fitted with Equation 2.4, where I_Γ and B_Γ are calculated and the only free parameter is Γ/Δ. For fields higher than 50 mT, the Usadel equation does not fit any more. For fields higher than 200 mT, the data follow the critical current.*

4.5.1 Temperature dependence

From the fits of the Anthore approximation of the Usadel equation to our data, we could extract the value of Γ/Δ for different temperatures. For 1.8 K, this value was $3.5 * 10^{-3}$ and for 5.5 K, it was $2.9 * 10^{-3}$.

4.6 Usadel on nanodetector

For the nanodetector, the values of I_Γ and B_Γ are different because of the difference in width and in resistance (see Table 3.1). In Figure 4.9 the current through the nanodetector is plotted as a function of magnetic field for a constant countrate of 1000 counts per second. The Anthore approximation of the Usadel equation can also be fit through these data well up to 60 mT. For 2 K, the value of Γ/Δ is $2.8 * 10^-3$.

Figure 4.9: *Current as a function of magnetic field for a constant countrate of 1000 counts per second on the nanodetector. The data are fitted with the Anthore approximation of the Usadel equation, where I_Γ=329 μA and B_Γ=1.879 T. The only free parameter is Γ/Δ.*

Chapter 5

Discussion on magnetic field experiments

5.1 Critical current and dark counts

We measured critical current as a function of magnetic field. However, the way we measured critical current is problematic. As mentioned before, we used a 10% resistance criterion, which gives us an of 10 Ω. At the temperatures we work at, this resistance changes with field: $R(B) = \frac{B}{B_{c2}}R(B_{c2})$. The resistance of the short wire in the normal state is approximately 50 Ω at zero field, so for 1 T, we try to detect a change in the resistance of the order of 5 Ω. The 10% resistance criterion to determine I_c introduces a systematic error, as the resistance curve depends on the magnetic field. Detection of the critical current should actually be done using a fourpoint measurement. Thus, we cannot be sure about our measurements of the critical current, especially for high fields.

   We found that two regimes can be distinguished in the dependence of the critical current of the magnetic field, namely a linear and a power law regime (see Figure 4.1). The same behavior has been seen before on different samples by Plourde et al[24], although the slope, the interception with the B axis and the power are different. Plourde reports a slope of -51 μm in the units used in [24], which can be rewritten to -41 mm/mT, and we measured -0.29 $\mu A/mT$ for 1.8 K and -0.19 $\mu A/mT$ for 5.5 K. Taking into account the differences in sample, calculation of this slope using the equation of [24] gives values of the same order of magnitude as we measure. They have an interception with the B axis at 2.8 mT, and we have it at 0.14 T. They measure a power of $x = $ -1, and we measure $x = $ -0.38 for 1.8 K and $x = $ -0.84 for 5.5 K. The samples they used were made out of a weak pinning superconductor, and we use a strong pinning superconductor. This could account for the quantitative differences in slope, interception with the

B axis and power. Qualitatively, we see the same shape of the curve. Inspired by [24], we attribute the linear regime to induced depairing of Cooper pairs, and the power law regime to flux flow. This means that the crossover between the two regimes happens because the edge barrier for the vortex entry is lowered by the magnetic field. Recalculation of the expected values and reconsidering the comparability of our sample with the ones that were used previously might lead to a better understanding of the behavior of the critical current as a function of magnetic field.

We measured the critical current as a function of magnetic field for different temperatures. The critical current in zero field is found to follow the Bardeen temperature dependence (see Figure 4.2). Questions about the temperature dependences of the slope, the interception with the B axis and the power of the power law regime remain open.

We found that dark counts increase exponentially with current (see Figure 4.3). This has been described earlier by Bulaevskii [12], although the current dependence that he calculates is twice as low as what we measure. A more precise calculation or a measurement of the London penetration depth of our sample could possibly provide a better estimate of the theoretically expected temperature dependent behavior. We found that dark counts follow the critical current (see Figure 4.4).

The exponent of the dark counts depends on the applied field. It is unclear from theory what dependence there is expected here. More measurements on different samples and at different temperatures could give a phenomenological dependence.

5.2   Light counts

We found that the light counts behave in an entirely different way than dark counts as a function of current (see Figure 4.3 and 4.5). This has been shown previously in meander samples, where this difference was attributed to detection of light counts at a different place in the sample than the detection of dark counts [6]. As our samples have only one active spot or area, we show that in our detection, this difference is due to an intrinsic difference between light and dark counts. It would be physically interesting to find out the origin of this difference. Actually, the shape of the pulses produced by light and dark counts are comparable in size and time scale.

We see three different regimes in the count rates as a function of magnetic field for different currents (see Figure 4.6). Light counts as a function of magnetic field have been predicted by Bulaevski to have only one regime with a cosh like behavior [12], which has an exponent of 10 mT. We see exponents of the order

or 22.4 mT for the first regime, 13.8 mT for the second regime and 45.4 mT for the third regime, which are all different than the theoretically predicted ones. A difference between the theorical and measured value of this exponent has been seen before, where no real field dependence was seen [6].

An important result we found is that for fields under the 50 mT, the Usadel equation fits our data for all the temperatures we measured at, and for both samples (see Figure 4.7 and 4.9). For these low fields, we expect to be in a homogeneous case. This means that current and magnetic field have a similar effect on the superconducting order parameter Γ, which means that Equation 2.4 is applicable. This equation describes the behavior of a superconductor under influence of current and magnetic field, but it also describes the behavior of the photon counts of our superconducting single photon detector very well. This is a striking result.

As mentioned before, we have measured light counts as a function of current and field for different temperatures. The fitted Γ/Δ is expected to be temperature dependent, which our data confirm. Since this theory is based on superconductive effects, there should be no wavelength dependence. Preliminary results show that there is indeed no dependence on the wavelength of the used light, but future experiments should be performed to confirm this statement.

As stated before, for fields above 50 mT we attribute the behavior of the critical current to flux flow. This means that for these fields, current and magnetic field influence the superconductor in a different way, as the magnetic field removes the edge barrier for vortices, and the current does not. For this inhomogeneous situation, the approximation leading to Equation 2.4 is not applicable any more. This can be seen from our data, where for fields above 50 mT, the equation does not fit any more. Calculation of the energy of the edge barrier could confirm that the crossover at 50 mT is really due to the dissapearing of an edge barrier.

In a magnetic field, light counts not only shift towards lower currents, but the shape of the light counts as a function of current changes to being more like the exponential shape of dark counts. For high fields, the current as a function of fields for constant count rates follows the critical current (see Figure 4.8). As dark counts follow the critical current, this is another reason to expect that light counts for high magnetic fields are actually dark counts. Future experiments of dark counts in high magnetic fields could provide information on the question of whether counts at high magnetic fields are dominated by dark counts.

Chapter 6

Results for polarisation experiments

6.1 Polarisation dependence of p_i and η

Apart from looking at the effect of magnetic field on the detector response, we have also looked at the effect of different polarisations of light on the detector response using tomography. This we did on a short wire sample of 100 nm length and 150 nm width (see Section 3.1). We measured at the base temperature of the cryostat, 3.1 K. We measured count rates as a function of current and used the tomography procedure to extract both the absorption probability η and the click probabilities p_i (see Section 2.3). We varied the laser power from pW to μW. This we did for different angles of the polarizer (see Section 3.4). We saw a clear difference of 20% between the highest and lowest value of p_1, with p_1 around 0.55 (for the statistical relevance of our data, see Section 6.3). For the intermediate polarisation angles, the value of p_1 interpolates nicely to form a sine (see Figure 6.1).

The same sine can be seen in the values for p_2 as a function of polarisation angle (see Figure 6.2). Here there is 38% difference between the highest and the lowest value, for p_2 around 0.3.
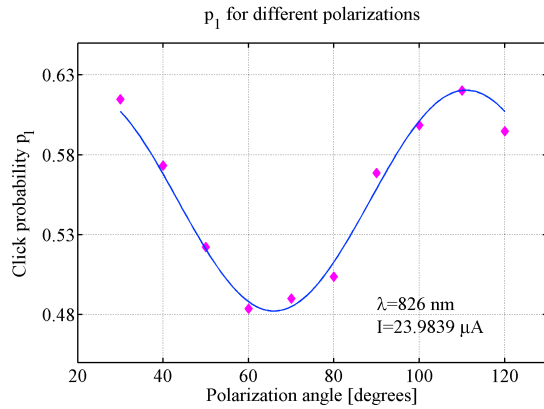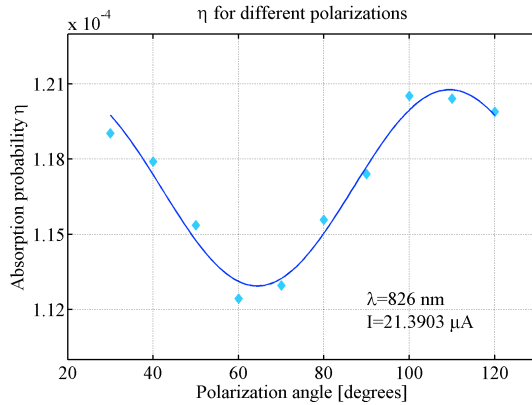
Figure 6.1: *Probability that the detector clicks for one photon, p_1, as a function of the polarisation angle, for a wavelength of 826 nm and a current of 23.9839 μA for short wire 1. The zero angle is chosen arbitrarily. There is 20% difference between the highest and the lowest value of p_1. A sine with a period of 90^0 is fit through the data points.*
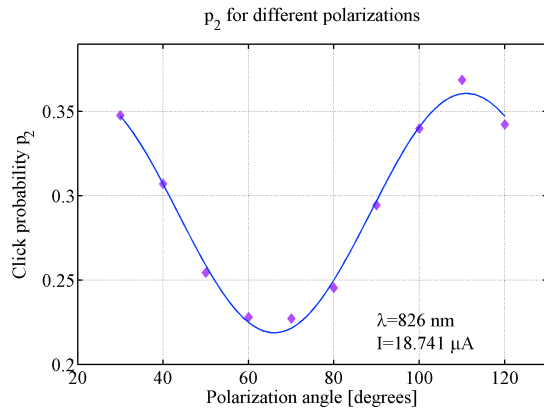
Figure 6.2: *Probability that the detector clicks for two photons p_2 as a function of the polarisation angle, for a wavelength of 826 nm and a current of 18.741 μA for short wire 1. The zero angle is chosen arbitrarily. There is 38% difference between the highest and the lowest value of p_2. A sine with a period of 90^0 is fit through the data points.*

Finally, the same sine can be seen in the values of η as a function of polarisation angle (see Figure 6.3). Here there is only 7% difference between the highest and the lowest value, for η around 1.15×10^{-4}.


Figure 6.3: *Probability that a photon is absorbed η as a function of the polarisation angle, for a wavelength of 826 nm and a current of 21.3903 μA on short wire 1. The zero angle is chosen arbitrarily. There is 7% difference between the highest and the lowest value of η. A sine with a period of 90^0 is fit through the data points.*

6.2   Visibility and wavelength

A natural thing to look at is the visibility of the sine signal for different parameters. Visibility is here defined as $(n_{max} - n_{min})/(n_{max} + n_{min})$. Figure 6.4 shows the calculated visibility of the polarisation dependence of p_1 versus current for various wavelengths. For higher currents, the visibility of the signal goes down to 0.05. For low currents, there is a difference between the visibilities for different wavelengths. The curve of the visibility at a wavelength of 500 nm starts at the lowest currents.

In the visibility of p_2, no real wavelength dependence can be seen (see Figure 6.5).

For the visibility of η, there is no real difference between the curves at 500 nm, 600 nm, 700 nm and 900 nm. The visibility for 826 nm is smaller than that of the other wavelengths (see Figure 6.6).
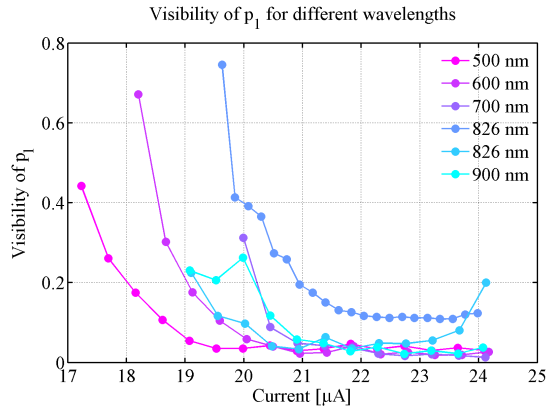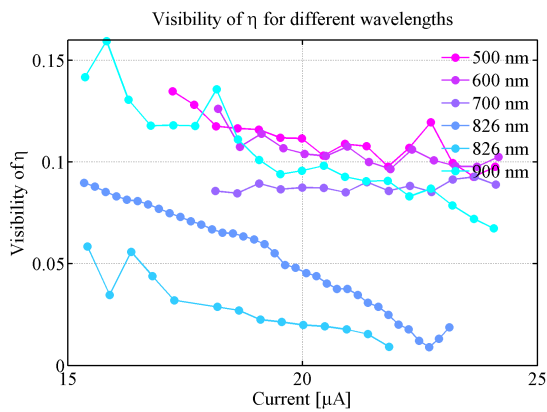

Figure 6.4: *Visibilities of p_1 as a function of current for different wavelengths on short wire 1. The visibility of the sine at 826 nm is maximal.*

6.3   Statistical relevance

The statistical relevance of our data was checked (see Figure 6.7). First a specific combination of p_1 and η belonging to a certain polarisation was chosen. The χ^2 using these calculated p_1 and η was calculated for the polarisation that was chosen. Than the same combination of p_1 and η was used to calculate the χ^2 of the other polarisations. The χ^2 belonging to the right combination of p_1 and η is five or six times smaller than the ones where the wrong values have been used.
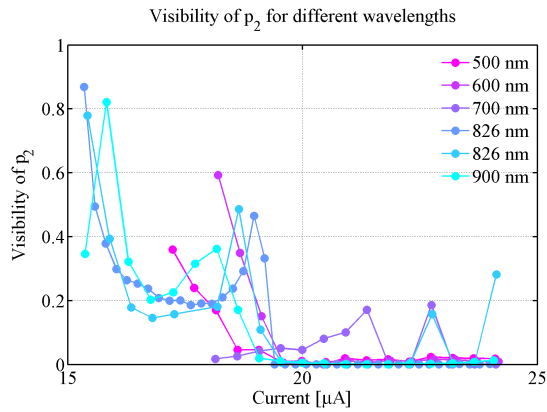
Figure 6.5: *Visibilities of p_2 as a function of current for different wavelengths on short wire 1. The visibility of the sine at 826 nm is minimal.*

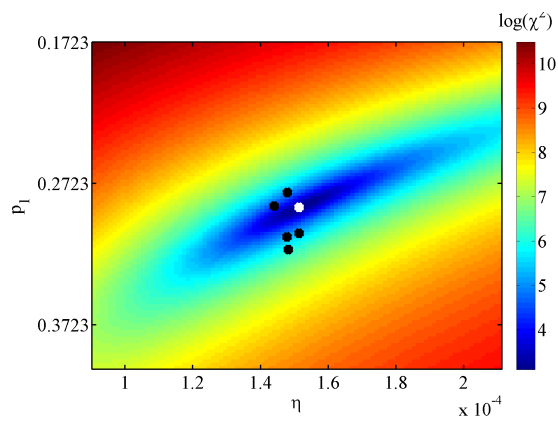**Figure 6.6:** *Visibilities of η as a function of current for different wavelengths on short wire 1. The visibility is minimal for 826 nm light.*

Figure 6.7: *Colorplot of χ^2 for different combinations of p_1 and η. The white dot belongs to the χ^2 which is calculated for the polarisation where the p_1 and η belonged to. The black dots indicate what the χ^2 is if this combination of p_1 and η was used to calculate the χ^2 for the other polarisations. The fact that there is such a difference in χ^2 and that they do not lie on one line indicates that our data are statistically relevant.*

6.4 High power and high current

For either high laserpower or high current, we saw a strange effect. Where the signal for low power and current had the form of a sine, for higher power or current it got an extra phase of π. This extra phase we saw both in the counts and in the calculated η as a function of polarisation. The p_i did not get an extra phase. In Figure 6.8) the visibility of the counts is plot for different combinations of laser power and current. This visibility changes sign for different regimes.
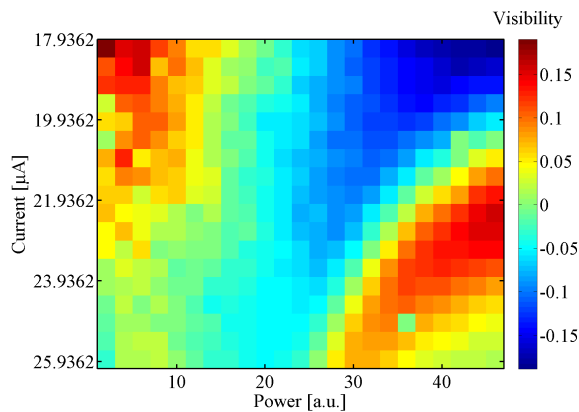
Figure 6.8: *Visibility of the counts for different combinations of current and power. For high power or high current, the visibility shifts sine. This means that the sine gets an extra phase of π.*

Chapter 7

Discussion on polarisation experiments

7.1   Wavelength dependence

Measurements have been done of absorption and click probability for light of different polarisations. We expected to see a clear difference in the response of the detector to different polarisations. This is indeed what we see both in the absorption efficiency η and the click probabilities p_1 and p_2.

Preliminary measurements have also been done on the wavelength dependence of this effect. What we first expected, is that the polarisation dependence would become stronger for shorter wavelengths. In Section 2.2.3 we mentioned two effects, namely the polarisation dependence of the absorption of the light, and the polarisation dependence of the click probability. The difference in click probability between the edge and the middle of the wire is predicted to be more for shorter wavelengths. On the other hand, the difference in absorption between the edge and the middle of the wire is predicted to be less for shorter wavelengths. Consequently, we expect that the visibility of the effect will become less for both shorter and longer wavelengths. However, we did not see a clear wavelength dependence.

7.2   Effects of high current and high power

For low currents and low powers, we saw that the sine of the counts, η and p_i all had the same phase. For high currents and high powers, we saw a strange effect in the data. First of all, we saw that the sine of the counts suddenly got an extra phase of π. The same thing happened to the sine of η, while the sine of p_i stayed the same. At the same time, we also saw that the current varied with the incident polarisation in a sinusoidal way in anti phase with the counts and η. This sine in the current had a peak to peak amplitude of the order of 20 pA. We attribute

this to an electronic problem. When the power is high, the detector clicks more often, so its mean resistance is higher. This means that the measured voltage is different than the real voltage over the detector. This sinusoidal behavior of the current could account for the change in phase in the counts versus polarisation. As the counts are a product of p_i and η, the change in phase in the counts results in a change in phase in η.

This strange effect could account for the fact that we do not see a clear wavelength dependence. We conclude that it is important to measure in the regime with low laser power. Taking this in mind, further measurements should be able to provide a better understanding of what happens.

Chapter 8

Conclusion

In conclusion, we investigated the behavior of superconducting single photon detectors in magnetic fields and their response to photons of different polarisations. We studied three different samples, namely a nanodetector of 220 nm width and two short wires of 150 nm width and 100 nm and 200 nm length. We study the count rate both in the dark and when illuminated with light at various bias currents. Further on, we vary either the magnetic field and the temperature and use a fixed wavelength of 826 nm, or we vary the polarisation and the wavelength of the light and use a fixed temperature of 3.1 K and no magnetic field.

Thus, we have demonstrated that there are two regimes in the critical current as a function of the magnetic field, namely a linear regime where there is induced depairing, and a power law regime with flux flow. For low fields up to 50 mT, the behavior of the light count rate can be described with the Usadel equation, because the magnetic field and the current influence the superconductivity in a similar way. The magnetic field dependence for low fields follows the temperature dependence of Δ. Dark counts behave entirely different than light counts, although in our sample they both are produced in a single active spot. Dark counts do not obey the Usadel equation, but follow the critical current. For fields above 200 mT, the count rate is dominated by dark counts.

Considering the polarisation dependence of the response of the detector, we have demonstrated that there is indeed a difference in absorption efficiency and click probability for different polarisations. Preliminary measurements on the wavelength dependence of this polarisation dependence show that unwanted effects occur when measuring at high laser power or high current. Further work should provide better understanding on how the difference in absorption and click probability for different polarisations depends on the used wavelength.

References

[1] Rose-Innes, A.C., Rhoderick, E.H., *Introduction to Superconductivity*, second edition, BPC Wheatons, Exeter, Great Britain, (1978)

[2] Semenov, A.D., Gol'tsman, G.N., Kornee, A.A., *Quantum detection by current carrying superconducting film*, Physica C 351, 349–356 (2000)

[3] Marsili, F., Verma, V.B., Stern, J.A., Harrington, S., Lita, A.E., Gerrits, T., Vayshenker, I., Baek, B., Shaw, M.D., Mirin, R.P., Nam, S.W., *Detecting Single Infrared Photons with 93% System Efficiency*, Nature Photonics 7, 210–214 (2013)

[4] Natarajan, C.M., Tanner, M.G., Hadfield, R.H., *Superconducting nanowire single-photon detectors: physics and applications*, Superconductor Science and Technology 25 (2012)

[5] Gol'tsman, G.N., Okunev, O., Chulkova, G., Lipatov, A., Semenov, A., Smirnov, K., Voronov, B., Dzardanov, A., *Picosecond superconducting single-photon optical detector*, Applied Physical Letters 79, 705–707 (2001)

[6] Engel, A., Schilling, A., Ilin, K., Siegel, M., *Dependence of count rate on magnetic field in superconducting thin-film TaN single-photon detectors*, Physical Review B 86, 140506 (2012)

[7] Engel, A., private communication

[8] Annet, J.F., *Superconductivity, Superfluids and Condensates*, Oxford University Press, New York, Unites States of America, 47–145 (2012)

[9] Tinkham, M., *Introduction to Superconductivity*, second edition, Dover Publications, Mineola, United States of America, 11–13 (2004)

[10] Anthore, A., Ponthier, H., Esteve, D., *Density of States in a Superconductor Carrying a Supercurrent*, Physical Review Letters 90, 12 (2003)

[11] Renema, J. J., Gaudio, R., Wang, Q., Zhou, Z., Gaggero, A., Mattioli, F., Leoni, R., Sahin, D., Dood, M.J.A. de, Fiore, A., Exter, M.P. van, *Experimental test of the detection mechanism in nanowire superconducting single photon detectors*, Physical Review Letters 112, 117604 (2014)

[12] Bulaevskii, L.N., Graf, M.J., Batista, C.D., Kogan, V.G., *Vortex-induced dissipation in narrow current-biased thin-film superconducting strips*, Physical Review B 83, 144526 (2011)

[13] Anant, V., Kerman, A.J., Dauler, E.A., Yang, J.K.W., Rosfjord, K.M., Berggren, K.K., *Optical properties of superconducting nanowire single-photon detectors*, Optics Express 16, 10750–10761 (2008)

[14] Driessen, E.F.C., *Coupling light to periodic nanostructures*, PhD thesis, Leiden University (2009)

[15] Wang, Q., private communication

[16] Engel, A., Schilling, A., *Numerical analysis of detection-mechanism models of superconducting nanowire single-photon detector*, Journal of Applied Physics 114, 21 (2013)

[17] Renema, J.J., Frucci, G., Zhou, Z., Mattioli, F., Gaggero, A., Leoni, R., Dood, M.J.A. de, Fiore, A., Exter, M.P. van, *Modified detector tomography technique applied to a superconductin multiphoton nanodetector*, Optics Express 20, 2806–2813 (2012)

[18] Bitauld, D., Marsili, F., Gaggero, A., Mattioli, F., Leoni, R., Nejad, S.J., Levy, F., Fiore, A., *Nanoscale Optical Detector with Single-Photon and Multiphoton Sensitivity*, Nanoletters 10, 2977-2981 (2010)

[19] Clem, J.R., Berggren, K.K., *Geometry-dependent critical currents in superconducting nanocircuits*, Physical Review B 84, 17 (2011)

[20] Kerman, A.J., Dauler, E.A., Yang, J.K.W., Rosfjord, K.M., Ananta, V., Berggren, K.K., Goltsman, G.N., Voronov, B.M., *Constriction-limited detection efficiency of superconducting nanowire single-photon detectors*, Applied Physics Letters 90, 101110 (2007)

[21] Rengelink, B., *Superconducting-nanowire-single-photon-detectors in a magnetic field*, master thesis, Leiden University (2013)

[22] Kralingen, M., *Temperature-dependence of NbN photon detector behavior*, bachelor thesis, Leiden University (2012)

[23] Bardeen, J., *Critical fields and currents in superconductors*, Journal of modern physics 34, 667–681 (1962)

[24] Plourde, B.L.T., Harlingen, D.J.van, Vodolazov, D.Y., Besseling, R., Hesselberth, M.B.S., Kes, P.H., *Influence of edge barriers on vortex dynamics in thin weak-pinning superconducting strips*, Physical Review B 64 (2001)

Lab View program for measuring with PPMS

A.1 Name

Uberprogramma_PPMS.vi

A.2 Purpose

The purpose of this program is to measure output voltage and photon counts as a function of input voltage.

A.3 Devices

This program is meant to control the following devices:
Yokogawa GS200
Agilent multimeter 34410A
Agilent frequency counter 53220A

A.4   Input

Start voltage (mV)	The voltage with which you want to start, in mV
End voltage (mV)	The voltage with which you want to end, in mV
Step voltage (mV)	The step size to go from one to another voltage in mV
# Times count pulses	The amount of pulses counted per voltage
Trigger level (V)	The trigger level you want the counter to react on in V
Saw tooth?	This gives a voltage shape which goes from up from start to stop and back
Inverted saw tooth?	This gives a voltage shape which goes down from start to stop and back to
Offset	It is possible to start the (inverted) saw tooth at some offset level
# repeat times	Whatever shape is chosen, it can always be repeated N times
Stop after Ic?	Whether you want the program to stop the moment the output voltage goe

A.5   Output

The graph voltage shape shows the shape of the output voltage as a function of time, which is especially handy if you have saw teeth or other strange shapes.

The graph I/V curve gives the input voltage in mV versus the output current in μA.

The graph Counts gives the average number of counts as a function of the input voltage in mV.

Counted pulses gives the counts at every moment in time they are being counted, so you can watch it.

Completion gives the completion of the most important loop in the program in %.

A.6   STOP

The STOP button is to be used to stop the program half way. This will enable you to save the data measured until then, and the devices will not give errors. Always use this one to stop!

A.7   Detailed description of the program

The program consists of a flat sequence structure with six frames.

Frame 1:   In the first frame, the session with the Yokogawa is opened. Afterwards, the output is put on. The program checks whether the output is really on.

Frame 2:   Here an array is made of the input voltages.

Sub VI create_omgekeerde_zaagtand   If the user has selected the inverted saw tooth, the sub VI create_omgekeerde_zaagtand is used. In this VI, an array of voltages is created using a while loop. This while loop starts from the start voltage and adds the step size times the index, until the end voltage is reached. The resulting array is multiplied by -1. Optionally, this saw tooth can be given an offset.

Sub VI volt_array   In this VI, the normal array of voltages is made. There are two options: either the start voltage is smaller than the end voltage, or vice versa. If you go from a high start voltage to a lower end voltage, the program starts with the start voltage and subtract the step size times the index, until the end voltage is reached. If you go from a low start voltage to a higher end voltage, the program adds the step size times the index to the start voltage until the end voltage is reached.

Sub VI create_zaagtand   If the user has selected the saw tooth, this sub VI uses the existing array of voltages. Then this same array is inverted in such a way that it starts with the last number and continues to the first number, is added to the original one. In this way, you get a saw tooth shape.

Sub VI Repeating_array   If you want to repeat any of the chosen shapes, this sub VI repeats the original volt array N times.

Sub VI Choose_range   In this VI, the maximum value of the voltage array is calculated. Based on this, the range of mV or V is chosen and made into a command, which can be sent to the Yokogawa.

Frame 3:   Now the sessions with the Agilent counter and Agilent multimeter are also opened. The counter is said to measure DC pulse with a resistivity of 50 ohms which have a negative slope.

Frame 4:   This frame contains the most important for loop with another sequence with five frames in it.

Frame 1 in loop: Here the voltage in V sent to the Yokogawa. The program asks the Yokogawa whether it is finished already, and proceeds only when it is done.

Frame 2 in loop: Here the voltages are read out from the Agilent multimeter.

Sub VI read_out_voltages: In this VI, the voltage is read out N times. Then the mean and standard deviation values are calculated. The answer is given in mV.

Frame 3 in loop: Here the correct trigger level is put on the Agilent pulse counter. Then the system waits for a certain time. The program proceeds only when the counter confirms that it is done.

Frame 4 in loop: Here the counter counts pulses for N times. It is measured using totalize, measuring for 1 second. The measured pulses are put in an array.

Frame 5 in loop: In this frame there is a STOP button, which can stop the program when the user wants it. In the rest of this large frame, there are three graphs being built. The upper graph is an I/V curve, where I is calculated using Ohm's law. The middle graph gives the voltage as a function of the index of the loop. This allows you to see the voltage shape. The lower graph plots the mean of the measured counts as a function of input voltage.

Stop after Ic   When the user selects this button, the program will stop when the voltage becomes lower than the previous voltage, so when the critical current is reached.

Completion   The completion is calculated dividing the index of the loop by N.

Frame 5:   In this frame, the input voltage, the measured current (or actually voltage times 10), the standard deviation of the measured voltage and the measured counts are written to a file. The sessions with the Agilent counter and Agilent meter are closed.

Frame 6:   In this frame, the output of the Yokogawa voltage source is stopped. Then the session with the Yokogawa is closed.

Lab View program for tomography measurements

B.1 Name

Uberprogramma_9e_2.vi

B.2 Purpose

The purpose of this program is to measure output voltage and photon counts as a function of input voltage and angles of $\lambda/2$ plates.

B.3 Devices

This program is meant to control the following devices:
Yokogawa GS200
Keithley multimeter 2000
Agilent frequency counter 53131A
Newport motion controller model ESP300

B.4   Input

Start voltage (mV)	The voltage with which you want to start, in mV
End voltage (mV)	The voltage with which you want to end, in mV, should be larger than th
Step voltage (mV)	The step size to go from one to another voltage in mV
# Times count pulses	The amount of pulses counted per voltage
Trigger level (V)	The trigger level you want the counter to react on in V
Start polarisation angle	The angle you want to start varying the polarisation with in degrees
End polarisation angle	The angle you want to stop varying the polarisation
Step polarisation angle	The step in angle you want to take
Start power angle	The angle you want to start varying your power with
End power angle	The angle you want to stop varying your power with
Step power angle	The step in angle you want to take

B.5   Output

The graph I/V curve gives the shape of the curve of the input voltage versus the output current.
The graph Counts gives the average number of counts as a function of the input voltage.
Completion gives the completion of the loop in %.

B.6   STOP

The STOP button is to be used to stop the program half way. Then you will be able to save the data measured until then, and the devices will not give errors. Always use this one to stop!

B.7   Detailed description of the program

The program consists of a flat sequence structure with six frames.

Frame 1:   In the first frame, the session with the Yokogawa is opened. Afterwards, the output is put on. The program checks whether the output is really on.

Frame 2:   Here an array is made of the input voltages and all angles, and the right range is put on the Yokogawa source.

Sub VI overkoepelend_array_2   This VI consists of three for loops in each other. In the inner for loop, an array is built with the input voltages. Another array is built using the index of the second loop, with the first angle (polarisation). A third array is built using the index of the third loop, with the second angle (power). In the middle loop, arrays are built using the arrays of the inner loop. In the third loop, arrays are built using the built arrays of the middle loop. Then these arrays are combined into a large array. The first column now gives the second angle. To change this order, it is enough to connect the wires in a different manner to this last Build array. This array is transposed at the end. Note that the program only works when you go from lower to higher voltage and angles.

Sub VI Choose_range   In this VI, the maximum value of the voltage array is calculated. Based on this, the range of mV or V is chosen and made into a command, which can be sent to the Yokogawa.

Frame 3:   Now the sessions with the Agilent counter, the Keithley multimeter and the ESP motion controller are also opened. The counter is said to measure DC pulses with a resistivity of 50 ohms, which have a negative slope and using the totalize function. The trigger level is put on the counter. The angle at which both $\lambda/2$ plates are at the current moment, are asked from the ESP.

Frame 4:   This frame consists of a for loop with another sequence of five frames in it.

Frame 1 in loop: In this frame, first the given value from the array is compared with the previous value of the angle. If the angles are the same, then nothing happens. If the previous angle minus the angle you want to put now, is smaller than the step size divided by 100, than the case structure happens. The first angle is compared with the value that the $\lambda/2$ plate already had in the beginning. In the case structure, the ESP is commanded to put its driver on the angle you want it to be on. After a minute, the program starts asking whether the task is completed yet. If the task is completed, the program goes on.

Frame 2 in loop: Here actually happens the same, but now with the other lambda/2 plate. So the angle is compared with the previous one, and if they are different, the driver changes the angle to the demanded one. When this task is completed, the program goes on.

Frame 3 in loop: Here the voltage in V sent to the Yokogawa, if the desired voltage is different than it was before. The program asks the Yokogawa, whether it is finished already, and proceeds only when its done.

Frame 4 in loop: Here the voltages are read out from the Keithley multimeter.

Sub VI read_out_voltages: In this VI, the voltage is read out N times (default 10). Then the mean and standard deviation values are calculated. The answer is given in mV.

Frame 5 in loop: Here the counter counts pulses for N times. It is measured using totalize, measuring for 1 second. The measured pulses are put in an array.

In the rest of this large frame, there are two graphs being built. The upper graph is an I/V curve, where I is calculated using Ohms law. The lower graph plots the mean of the measured counts as a function of input voltage.

Completion The completion is calculated dividing the index of the loop by N.

Frame 5: In this frame, the input voltage, the input angle 2, the input angle 1, the measured current (or actually voltage times 10), the standard deviation of the measured voltage and the measured counts are written to a file.

Frame 6: In this frame, the output of the Yokogawa voltage source is closed. The sessions of the Yokogawa source, the Agilent counter, the Keithley meter and the ESP motion controller are closed.